Corrosion Science 80 (2014) 104–110

Contents lists available at ScienceDirect

Corrosion Science

journal homepage: www.elsevier.com/locate/corsci

The role of constituent phases on corrosion initiation of NiAl bronze in acidic media studied by SEM–EDS, AFM and SKPFM

Davood Nakhaie *, Ali Davoodi, Amin Imani

Materials & Polymers Engineering Department, Faculty of Engineering, Hakim Sabzevari University, Sabzevar, Iran

ARTICLE INFO

Article history:
Received 11 August 2013
Accepted 16 November 2013
Available online 23 November 2013

Keywords:
A. Copper
B. AFM
B. SEM
C. Acid corrosion

ABSTRACT

Scanning electron microscopy (SEM), atomic force microscopy (AFM) and scanning Kelvin probe force microscopy (SKPFM) were used to examine the role of constituent phases of a NiAl bronze in corrosion initiation in HCl solution. Volta potential revealed anodic character of κ phases with tens of mV higher than copper rich α phase as cathodic matrix. A correlation between SKPFM results and Work function values of constituents was obtained. SEM and AFM images revealed that the iron rich κ phases are the most preferential sites for corrosion initiation.

1. Introduction

Nickel–aluminum bronzes (NAB) are widely used in marine environments due to their high mechanical properties, good corrosion and biofouling resistance [1–3]. Generally, in as cast condition the microstructure of NAB includes copper rich α grains, retained martensitic β and four nickel–iron–aluminum phases known as κ [1–4]. Based on the heat treatment history the alloy contains a vast spectrum of different microstructures. Depending on heat treatment conditions, the volume ratio and the chemical composition of the constituent phases can be adjusted to yield different properties [5,6]. It has been reported that the precipitation of κ phases in the α matrix significantly increases the strength [2], however, inhomogeneous distribution of these phases in cast NAB promotes the corrosion susceptibility of the material [7].

The presence of aggressive species in sea water, Cl^- in particular, makes the corrosion of the engineering components made form NAB inevitable. From this point of view, the corrosion behavior of NAB has been the subject of several researches [2,8–10]. Wharton et al. studied the crevice corrosion behavior of the NAB [10]. Their results showed that the crevice corrosion was initially restricted to the eutectoid regions with a slight attack of the copper rich α phase within the $\alpha + \kappa_{III}$ eutectoid. These results are consistent with findings reported by other researchers, which indicate an initial corrosion attack of α phase within the $\alpha + \kappa_{III}$ eutectoid in NaCl solution [2,11].

To improve wear and corrosion resistance of a cast NAB employing inorganic and metallic coating has been proposed [12]. Moreover, it has been shown that the modification of the microstructure of a cast NAB by friction–stir processing (FSP) enhances the corrosion behavior of the alloy in 3.5% NaCl solution. The morphological changes of κ phases during FSP together with alleviation of the segregation increase the corrosion resistance [7]. Based on microstructural examination of specimen surface immersed in seawater, it has been reported that κ precipitates are cathodic with respect to copper rich α [2,11].

Scanning Kelvin probe force microscopy (SKPFM) is developed for simultaneously mapping of topography and Volta potential distribution on conductive materials surfaces in the air [13]. It associates the classical scanning Kelvin probe method with atomic force microscopy (AFM). This method has a high resolution of ca. 1 mV in reading the surface potential.

Although considerable researches have been devoted to investigate the corrosion resistance of nickel–aluminum bronzes in saline water, to our knowledge, no attempt has been made to examine the role of the relative potential of different phases in corrosion initiation. The primary focus of this paper is on using local probing techniques to address the relative nobility and importance of constituent phases in corrosion initiation of a NAB alloy in chloride containing acidic solution.

2. Experimental

The nickel–aluminum bronze was received as a sand cast cylinder with diameter of 2.5 cm. The chemical composition of the alloy is given in Table 1, which is belonged to the ASTM B505. The micro-

* Corresponding author. Tel.: +98 5714003536; fax: +98 5714003520.
E-mail address: d.nakhaie@hsu.ac.ir (D. Nakhaie).

0010-938X/$ - see front matter © 2013 Elsevier Ltd. All rights reserved.
http://dx.doi.org/10.1016/j.corsci.2013.11.017

Table 1
Chemical composition of the NAB alloy (in wt%).

Al	Mn	Fe	Ni	Cu
10.5	1.05	4.5	4.95	79

structure and chemical composition of the phases present in the alloy was studied using Leo 1450VP scanning electron microscopy (SEM) equipped with quantitative energy dispersive spectroscopy (EDS). To characterize the microstructure of the cast NAB specimen was prepared with conventional metallography method and was etched in 10 wt% $FeCl_3$. Another sample was prepared and immersed in 0.1 M HCl for 30 s to disclose the preferential sites of corrosion initiation in acidic media. Backscattering Electron (BSE) images were obtained for the first specimen and Secondary Electron (SE) images were acquired for the latter one. Also, optical microscopy (OM) images were obtained in as polished condition.

Topography and Volta potential images were occupied using a commercial Solver Next AFM instrument (NT-MDT) from the mirror-like as polished surface. Since the relative humidity directly affects the Volta potential values,[14], all mappings were accomplished in the air at room temperature under controlled relative humidity of 20 ± 5 percent. The AFM tip was an n-type antimony doped silicon pyramid single crystal, which was coated by conductive PtIr (25 nm) and Cr adhesive layer (2.5 nm). The mapping of the surface Volta potential was conducted by using a two-pass technique; i.e. each line of the image was scanned twice. In the first step of scan process, there is no external voltage for applying to the tip. However, the line topography is recorded using the tapping mode technique and AFM plots the topography image from the sample surface. In the second pass the data which recorded in the first pass have been used during the second pass of scanning where a DC bias potential and an oscillating AC potential is applied to the tip. In the second pass the tip is lifted to a certain distance. Also, a feedback loop that controls the Z Piezo-device is turned off during this pass. So, the mapping of surface potential and topography is performed line by line in this procedure. In the present study, for Volta potential mapping, the lift scan height was 40–60 nm (depending on the surface roughness). Topography and Volta potentials were scanned with a pixel resolution of 256 × 256 and a scan frequency rate of 0.3 Hz. Since the actual Volta potential is the inversion of measured potential difference determined via SKPFM [14], all shown Volta potential images are the invert of measured potential.

3. Results

3.1. Microstructure

Fig. 1 shows the microstructure of the NAB alloy in as cast condition. As can be seen, the alloy microstructure comprises vast constituent phases. These phases, indicated as α, β, κ_I, κ_{II}, κ_{III} and κ_{IV} in the Fig. 1, are typical phases found in cast NAB [1]. The microstructure mainly includes grains of copper rich solid solution α phase, some portion of retained β and four κ phases distinguished by their morphology. The dendritic κ_I is rich in iron and was precipitated from β during cooling. The κ_{II} is also iron rich and dendritic-shaped, however, is smaller and more globular than κ_I. The lamellar κ_{III}, which has been shown to be NiAl intermetallic, is the product of eutectoidal transformation of β at lower temperature [4]. There is also another fine precipitate, κ_{IV}, which is distributed in α grains and is believed to be iron rich [1]. The average chemical composition of phases found in the alloy is listed in Table 2. The results are in good agreement with literature [1,4]. Since the κ_{IV} phase was found to be in submicron scales, and because of instrumental limitations, the elemental analysis of this phase was accompanied with considerable deviation. Therefore, it has not been shown in Table 2.

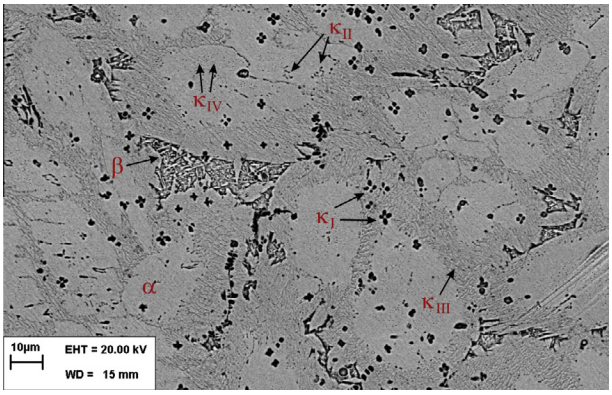

Fig. 1. BSE–SEM image of the investigated NAB alloy, etched in 10% $FeCl_3$, constitutive phases are indicated.

Table 2
The average chemical composition (in wt%) of constituent phases of the NAB alloy.

Phase	Chemical composition (in wt%)				
	Al	Mn	Fe	Ni	Cu
α	8.37	1.01	2.15	2.73	85.74
β	8.20	1.06	1.99	2.75	86.00
κ_I	13.97	1.36	46.9	16.17	21.58
κ_{II}	17.77	1.19	29.72	24.45	26.87
κ_{III}	18.21	1.03	13.82	28.34	38.45

3.2. AFM and SKPFM analysis

Fig. 2 represents the OM, AFM and SKPFM images of two separate regions recorded on polished surface of NAB. Fig. 2a–c shows OM and concurrent AFM topography and Volta potential images obtained from same area. The brightness of different zones in topographic images shown in Fig. 2 is matched with the difference in the heights of features on the sample surface. In other words, bright zones are higher than dark ones on the topographic maps. In a similar way, the brightness on Volta potential images is corresponding with different Volta potentials of the features shown on the Volta potential image, i.e. shiny areas have higher Volta potentials than the dark ones. Similar observations were recorded for another region as shown in Fig. 2d–f.

Almost all microstructural features represented in SEM micrograph (Fig. 1), including α grains, rosette-like κ_I, globular κ_{II}, and lamellar κ_{III}, can be discerned in Fig. 2a and d. It should be noticed that, the κ_{IV} is smaller than the spatial resolution of the topographies and Volta potential maps in Fig. 2. Therefore, this phase cannot be perceived. Since the OM images were obtained from as polished surface, special filters have been employed to signalize the microstructural features. Therefore, optical contrast resulted in better characteristic between different phases. Comparing topographic images with their corresponding OM micrographs, a slightly protuberant from the surface can be visible. Because the intermetallic κ phases are harder than the solid solution α matrix [2], they have lower rates of polishing. Consequently, these regions protrude from polished surface. Quantitatively, the maximum height differences on topography are reported to be c.a. 200 nm and the intermetallic phases' height are normally 20–40 nm higher than the matrix.

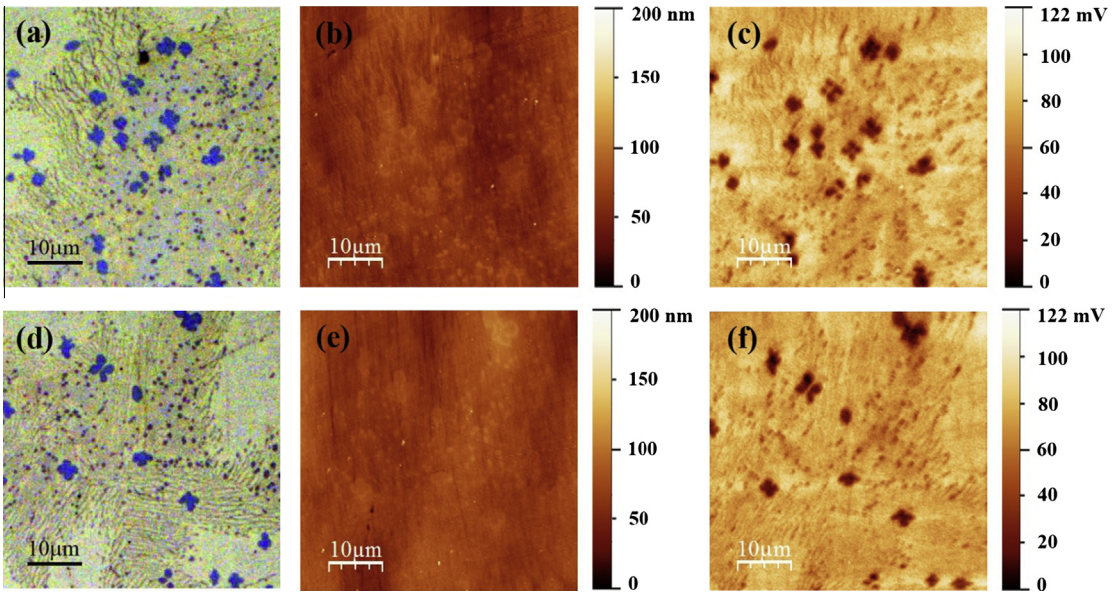

Fig. 2. (a) OM micrograph, (b) topography and (c) Volta potential images of a random region 1; (d) OM micrograph, (e) topography and (f) Volta potential images of random region 2. All images were obtained from as polished surface of the NAB alloy.

Nearly all of the κ phases seen in OM images can be easily distinguished in Volta potential maps. As mentioned in Section 2, actual Volta potential is the inversion of the measured potential difference determined via SKPFM [14], the Volta potential images shown in Fig. 2 are the invert of measured potential. As shown in Fig. 2a and b the κ_I dendrites appear to be the darkest characteristics in SKPFM images that imply they have the most negative potential among other constituents. This indicates the anodic behavior of κ_I phase in the localized corrosion process. The maximum Volta potential differences depicted by Fig. 2c and f are 122 mV with highest value corresponding to α grain and lowest value related to κ_I. This is an important result, since it is an indication of surface heterogeneity for localized corrosion attack.

To investigate the distribution of potential in more details, two line profiles, histogram and its deconvolution into multimodal distribution of Volta potential map are presented in the Fig. 3b and c, respectively. The positions of the profiles are indicated in the Fig. 3a. The line profile 1 depicts the Volta potential of an α grain, α + κ_{III} eutectoid and κ_I dendrite. In this profile the Volta potential begins from 80 mV over the α grain, decreases to 65 mV in the eutectoidal region, followed by sharp decrease to less than 5 mV, which designates the κ_I phase. The line profile 2 shows the variation of Volta potential from an α grain, a κ_I dendrite and two κ_{II} globules. Accordingly, in the profile 2 three distinct features can be identified. The potential starts around 80 mV, drops sharply to 55 mV, then increases to its early value of 80 mV, followed by steep fall to 5 mV and another local minimum of 55 mV. Comparing to OM image of Fig. 2a, three minimums in the profile 2 can be interpret as κ_{II}, κ_I and another κ_{II} phases, respectively. As it can be seen, in both profiles the lowest potential corresponds to κ_I. Moreover, κ_{II} possess the second lowest Volta potential.

It has been reported that conventional polishing may affect Volta potential values [15]. As wet polishing method was employed for sample preparation in the present study, the quantitative analysis of Volta potential must be taken cautiously. The relative nobility of the microstructural constituents is expressed as ΔE, which is defined as the difference between the potential of each κ phases and α matrix. ΔE is not easily influenced by test conditions. Therefore, this parameter may be regarded as a mean to assess the driving force for micro-galvanic in localized corrosion [16]. As revealed by the Fig. 3b, ΔE between the highest Volta potential (α phase) and the lowest Volta potential (κ_I phase) is about 75 mV. The Volta potential values of microstructural constituents can be summarized as follow:

$$\Delta E_{\kappa_I} < \Delta E_{\kappa_{II}} < \Delta E_{\kappa_{III}} < \Delta E_{\alpha} \approx \Delta E_{\beta} \quad (1)$$

And for κ_I adjacent to α matrix:

$$\Delta E_{\kappa_I} \ll \Delta E_{\alpha} \quad (2)$$

3.3. Corrosion initiation

Fig. 4 depicts the SE-SEM image of the NAB alloy which was immersed in 0.1 M HCl solution for 30 s. It is clear that the corrosion attack, i.e. metal dissolution, took place at three phases; the κ_I dendrites, κ_{II} globules and fine κ_{IV} precipitates. These darker regions are remained area implying the dissolution of intermetallic phases from the alloy surface. On the other hand, the κ_{III} lamellas remained unattacked. The dissolution of κ_I was more severe, particularly in the middle of the dendrite. Same findings of corrosion initiation at iron rich κ phases in chloride containing acidic media has been reported [17].

The topographic map of the specimen after exposure to 0.1 M HCl solution for 30 s is shown in Fig. 5a. Three dendrites of κ_I and some fine κ_{IV} particles can be identified by their morphological characters. These features are seemed darker compared with the matrix. The bright areas adjacent to the κ_I phases in Fig. 5a are most likely deposited dissolution products, due to enhanced local dissolution in the α/κ_I boundary region. Two line scans marked in Fig. 5a are shown in Fig. 5b. The profile 1 shows the depth of dissolution, which is about 53 nm. As it was shown previously in Section 3.2, the κ_I rosettes are higher than the α matrix, about 20–40 nm. This means that dissolution height is higher than 70–90 nm. Concerning the dimensions of dissolved κ_I phase, i.e. diameter of 4–5 μm compare to height of 70–90 nm, it is most likely that this phase has dish-shape character. Moreover, the EDS analysis at the center point of the dissolved phase showed similar composition to the matrix, which reveals the low height to surface aspect ratio of this phase and confirms its dish-shape character.

Some pit-liked features in Fig. 5a can be seen. The profile 2 in Fig. 5b provides topographic line scan over one of them. The profile shows that the diameter of the pit is less than 1 μm and its depth is about 12 nm.

4. Discussion

Nickel–aluminum bronze possesses complex microstructure characteristics, which intensely influence the alloy corrosion resistance. SKPFM is a powerful instrument to study the effect of microstructure on the corrosion behavior of such multi-phase alloy. In the present study, the relative nobility of microstructural constituents of a cast NAB are investigated to clarify the preferential sites of corrosion initiation in chloride containing acidic media.

4.1. Microstructure

The results of SEM investigation indicate, overall, that the microstructure of NAB includes six distinct phases of α, β, κ_I, κ_{II}, κ_{III} and κ_{IV}. These constituents phases are the characteristic microstructure found in a sand cast nickel–aluminum bronze [1,4]. According to experimental observations, the phase transformation sequence of cast NAB has been reported as follow. First the solidified alloy as single phase β transforms to copper rich α. Then, rosette-shaped iron rich κ_I precipitates in both α and β. By further

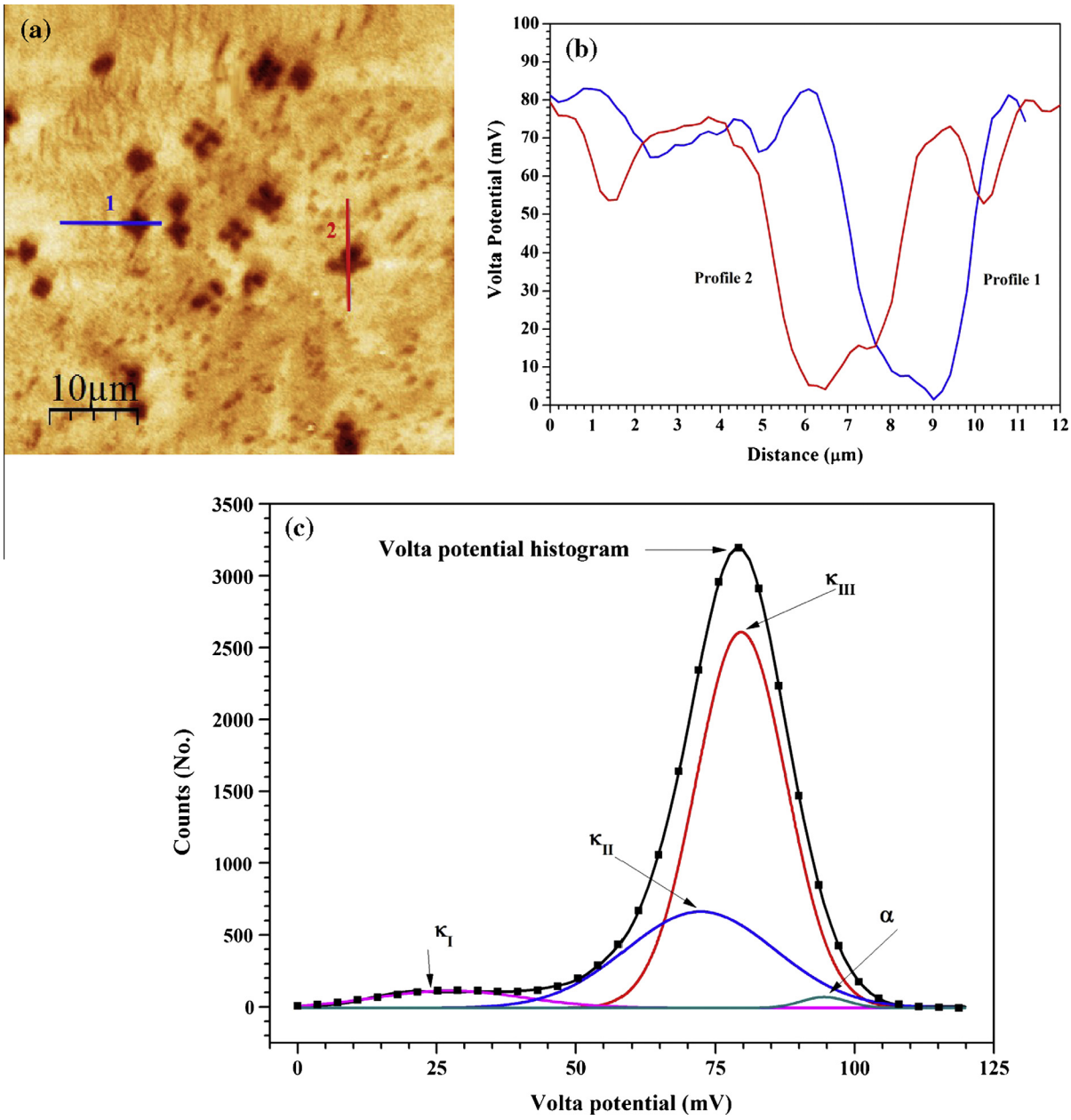

Fig. 3. (a) Volta potential map, (b) two line profiles and (c) deconvoluted histogram of Volta potential map. The histogram represents simulated multimodal Gaussian distribution of Volta potential corresponding to image (b). Each peak represents corresponding constituent phase which is indicated based on the probabilities of Volta potential data.

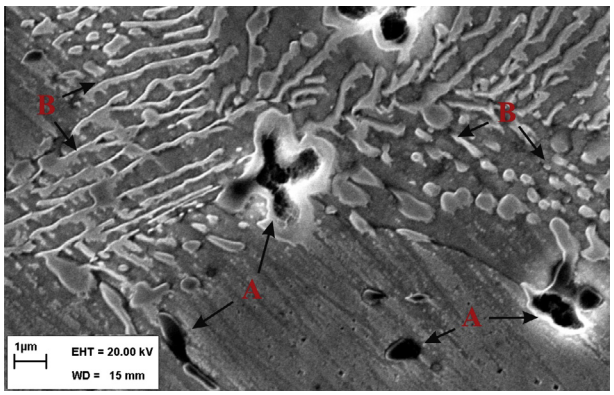

Fig. 4. SE-SEM image of the NAB alloy, immersed in 0.1 M HCl for 30 s. The corroded regions and the unattacked regions are indicated with letters A and B, respectively.

cooling, globular κ_{II} and lamellar κ_{III} form from β. Finally, precipitation of iron rich fine particles of κ_{IV} takes place [1,4].

4.2. Volta potential

SKPFM allows direct measurement of the local Volta potential values resulting from complex microstructure of the NAB alloy. The absolute values of potential are sensitive to many parameters and require careful measuring and instrument calibration. Therefore, the discussion is focused on the relative Volta potential between different phases. The Volta potential difference between the κ_I and α matrix is just locally more than 75 mV. This is more enhanced in histogram graph represented in Fig. 3c. In addition, the deconvolution of Volta potential histogram into the multimodal Gaussian revealed the presence of four components on the alloy surface, confirming the SEM–EDS results in Fig. 1 and Table 2. In other words, it is possible to recognize the constituents from the deconvoluted Volta potential histogram. Furthermore, deconvoluted graphs show the average values of Volta potential for constituents as 94, 79, 72 and 24 mV for α, κ_{III}, κ_{II} and κ_I, respectively. Again, in the case of α/κ_I galvanic couple, an average driving force of about 70 mV is predicted. In addition, the standard deviation of deconvoluted graphs for α, κ_{III}, κ_{II} and κ_I from the average values reveals information on the upper and lower limits in the chemical composition of these phases.

A much higher differences have been observed for intermetallic particles in Al alloys and nitride particles in Fe–Cr–V–N alloy [13,16,18]. It is worth to mention that, in these cases the second phases showed cathodic behavior compare to matrix, while in the investigating NAB alloy all κ phases possess more negative potential than α matrix, which makes them anode relative to matrix. It has been reported that the κ precipitates are cathodic with respect to copper rich α [2,11]. Visual inspection of corroded specimen surface in seawater, where the α grains have been dissolved and the κ phases were remained intact had led to such conclusion. However, the SKPFM results in the present study clearly show that all κ phases have negative Volta potential compare to the α matrix.

The dependence of Volta potential differences of κ phases could be attributed to their chemical composition. Previously, it is explained that κ phases transform from either β or α during cooling of the alloy. As Table 2 shows, different κ phases have different composition. While κ_I and κ_{II} are iron rich, κ_{III} is believed to be based on NiAl [4]. The reason for different Volta potential of the κ phases is probably related to the difference in iron, aluminum and copper contents of these constituents. According to the results represented in Table 2, it seems that iron as alloying element has the most deteriorative effect of corrosion properties of κ_I. On the other hand, copper increases the nobility of various phases.

It is established that the corrosion resistance is proportionally related to the Work function of elements [13,14]; the higher Work function, the higher corrosion potential. Accordingly, to find a correlation between microstructural constituents, their chemical composition and measured Volta potential values, the following linear equation is simply used as theoretical Work function values:

$$W = \frac{\sum_i W_i \times a_i}{\sum_i a_i} \tag{3}$$

where W is the Work function of microstructural constituents, W_i is the Work function of element i, extracted from [19], and a_i is the atomic percent (at%) of element i. Table 3 shows the calculated Work functions of α, β, κ_I, κ_{II} and κ_{III}. From the results in Table 3, meaningful differences can be resolved and the following outcome can be concluded:

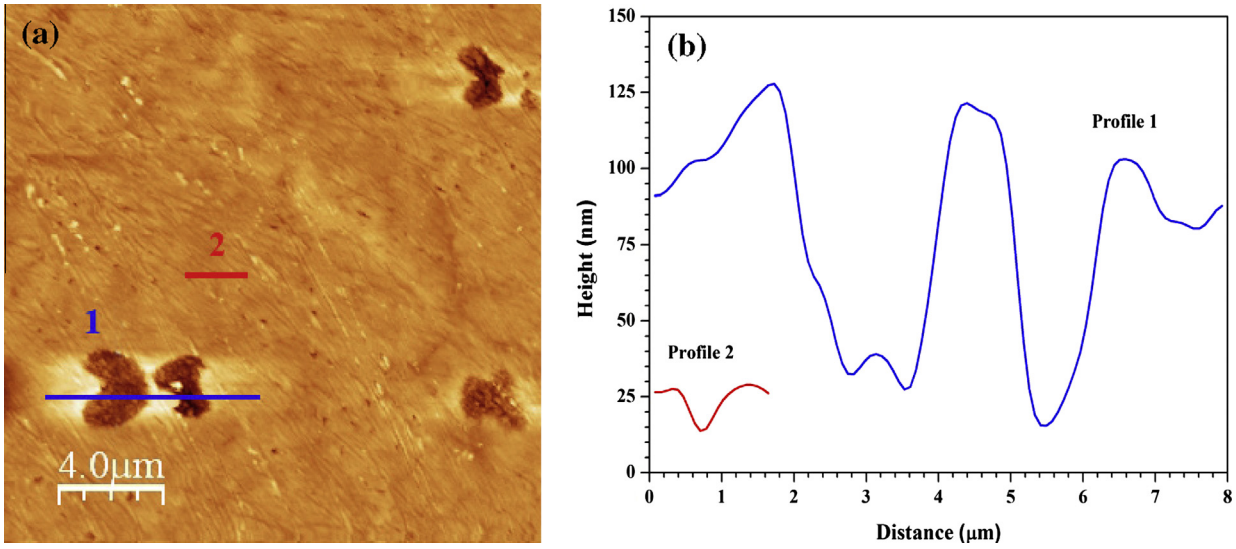

Fig. 5. (a) AFM topography image of the NAB alloy after immersion in 0.1 M HCl for 30 s, (b) two line profiles. The line profile 1 indicates height across a κ_I phase and the line profile 2 shows the height across a κ_{IV} phase.

Table 3
The average chemical composition (in at%) and calculated Work function of constituent phases of the NAB alloy.

Phase	Chemical composition (in at%)					Calculated work function (eV)
	Al	Mn	Fe	Ni	Cu	
α	3.75	0.92	1.99	2.66	90.65	4.672
β	3.67	0.96	1.84	2.68	90.82	4.672
κ_I	6.99	1.38	48.61	17.57	25.42	4.562
κ_{II}	8.96	1.22	31.03	26.83	31.93	4.591
κ_{III}	9.05	1.04	14.22	30.65	45.02	4.626

$$W_{\kappa_I} < W_{\kappa_{II}} < W_{\kappa_{III}} < W_{\alpha} \approx W_{\beta} \quad (4)$$

Therefore, the Eq. (4) confirms the trends of variation in measured Volta potential in Eq. (2). Fig. 6 shows the correlation between Volta potential in Fig 3b and Work function of different phases calculated by Eq. (4). Moreover, from best linear fit the Volta potential of pure elements were estimated. The trend of variations is similar to previously reported results [13,14,20]. Interestingly, the graph clearly shows that the Volta potential values of all constituents lay between iron and copper. This implies the importance of these two key elements.

Although it is acknowledged that the Work function values are reported in vacuum, the present Volta potential values are measured in air with relative humidity of 20 ± 5 percent and the corrosion tendency of microstructural constituents are reported in 0.1 M HCl solution after 30 s exposure, however, the results of Figs. 3, 4 and Table 3 are consistent. In other words, there is a good agreement between the SKPFM Volta potential values, SEM image and calculated Work function values. It should also be mentioned that, the chemical composition of constituent phases may change due to initial alloy composition, solidification processes and subsequent heat treatment. This can be seen in deconvoluted Volta potential histogram, as shown in Fig. 3c. As a result, the Volta potential values of different phases are composition dependent parameter. However, it is expected that the Eq. (4) is generally valid, despite that it has been previously reported not all κ_I dendrites are preferentially dissolved [17].

4.3. Corrosion initiation

It was shown that the dissolution behavior of NAB is pH dependent [17]. In near neutral chloride containing solutions the corrosion attacks take place at the α phase within α + κ_{III} eutectoid. In this condition, the κ_I has been scarcely affected and usually remains within corroded regions [10,17]. On contrary, for a manganese-nickel–aluminum bronze immersed in NaCl solution the first sign of corrosion initiation was observed at the κ_I phase [21].

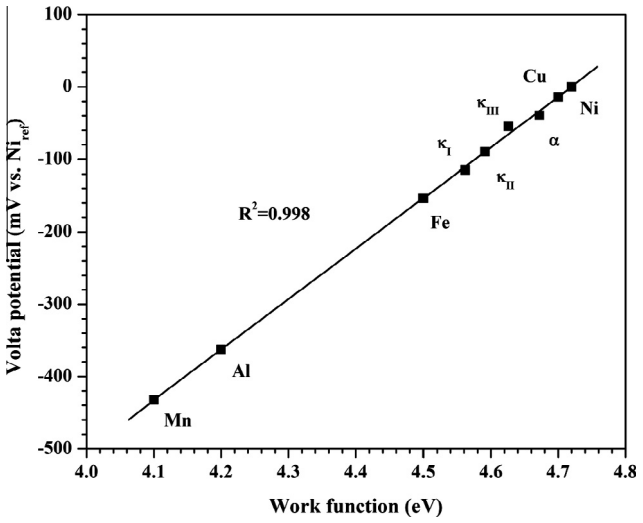

Fig. 6. Volta potential versus work function of different phases calculated by Eq. (4) and estimated Volta potential of pure elements with respect to Ni reference.

In the present study, the corroding sites are most likely related to the anodic κ phases, which have sufficiently low Volta potential differences compare to α matrix. Among κ intermetallics, κ_I shows the most negative Volta potential. Correspondingly, the anodic dissolution initiates from the κ_I. The deposition of corrosion products at the boundary region of κ_I could have been the result of such dissolution, as shown in Fig. 5a.

X-ray photo-electron spectroscopy analysis has been shown that the corrosion product film formed on α-Al bronze is a duplex layer of an inner adherent layer of Al_2O_3 and an outer layer of Cu_2O [22]. Furthermore, it was shown that the formation of Cu_2O relies on the relative chloride ion concentration and pH, with higher pH facilitates Cu_2O formation [23]. Using X-ray technique and Auger electron microscopy it has been observed that the anodic passivation of a NAB alloy in synthetic seawater is due to the formation of an aluminum-oxide protective film, which acts as a barrier for ionic transport across the corrosion products [8,9]. It was proposed that hydrolysis of complexes within the crevice results in the acidification of the crevice solution for a NAB alloy in NaCl solution [10]. Moreover, the aluminum oxide/hydroxide film becomes unstable below pH ca. 4. Consequently, the protective layer of the κ-phases due to their higher aluminum contents is lost and hence, the κ phases become anodic to the copper rich α phase.

According to present discussion, when the nickel–aluminum bronze is subjected to Cl^- containing acidic solution, both protective Al_2O_3 and Cu_2O oxides are not stable and undergo dissolution. In this condition, the dissolution of κ_I is more prone. Since the surface area of κ_I dendrites is significantly less than that of the matrix, according to galvanic corrosion principle, the rate of dissolution of this phase will be considerable. In other words, a small anode (κ_I) is in contact with a large cathode (matrix). Consequently, due to the electron neutrality the anode is polarized in more extent, which results in its accelerated dissolution. It can be deduced that despite the maximum Volta potential differences between constituents of NAB are about tens of mV, because of difference in surface areas of various phases, it still enough to create micro-galvanic cell and accelerates the dissolution of anodic iron-rich κ phases.

Likewise κ_I, the κ_{II} and κ_{IV} are iron rich phases. The chemical composition of κ_{IV} [1], suggests that the Volta potential of this phase could be as negative as the κ_I. The κ_{IV} precipitates are considerably finer than κ_I dendrites. Therefore, at a given immersion time the κ_{IV} precipitates could dissolve as shown in Fig. 4.

In summary, from corrosion point of view, the iron rich intermetallics are the most deteriorative phases. Therefore, as a suggestion, subsequent heat treatments which lead to diminish the above constituents are desirable. This study has addressed only the question of relative nobility of constitutive phases in a cast NAB alloy and the preferential sites of corrosion initiation in acidic solution. The SEM images together with topography image of immersed specimen in HCl solution clearly revealed that corrosion begins

at κ_I, κ_{II} and κ_{IV} phases, which is in accordance with SKPFM results. Nonetheless, as it has been observed by others, the preferential sites for corrosion initiation in near neutral Cl^- containing solution is the α phase within $\alpha + \kappa_{III}$ eutectoid. To clarify detailed explanation of the pH dependence of corrosion behavior of NAB (for instance, studies in NaCl solution) is desirable. Further studies are also necessary, using in-situ AFM, electrochemical atomic fore microscopy and scanning electrochemical microscopy [24–26].

5. Conclusion

AFM, SKPFM and SEM have been employed to map relative cathodic and anodic activity and to evaluate practical nobility of constituent phases of a nickel–aluminum bronze in corrosion initiation in HCl solution.

The Volta potential maps revealed the anodic character of κ phases (a value of tens of mV depending on chemical composition) relative to copper rich α phase. Among intermetallic κ phases, the κ_I showed the most negative Volta potential. Moreover, a correlation between SKPFM results and theoretical Work function values of alloy's constituents was obtained. SEM micrographs and AFM topography images disclosed that generally the iron rich κ phases are the most preferential sites for corrosion initiation, which confirmed the SKPFM results.

References

[1] E.A. Culpan, G. Rose, Microstructural characterization of cast nickel aluminium bronze, J. Mater. Sci. 13 (1978) 1647–1657.
[2] E.A. Culpan, G. Rose, Corrosion behaviour of cast nickel aluminium bronze in sea water, Br. Corros. J. 14 (1979) 160–166.
[3] G.W. Lorimer, F. Hasan, J. Iqbal, N. Ridley, Observation of microstructure and corrosion behaviour of some aluminium bronzes, Br. Corros. J. 21 (1986) 244–248.
[4] F. Hasan, A. Jahanafrooz, G.W. Lorimer, N. Ridley, The morphology, crystallography, and chemistry of phases in as-cast nickel–aluminum bronze, Metall. Trans. A 13 (1982) 1337–1345.
[5] M.D. Fuller, S. Swaminathan, A.P. Zhilyaev, T.R. McNelley, Microstructural transformations and mechanical properties of cast NiAl bronze: effects of fusion welding and friction stir processing, Mater. Sci. Eng., A 463 (2007) 128–137.
[6] D.R. Ni, P. Xue, D. Wang, B.L. Xiao, Z.Y. Ma, Inhomogeneous microstructure and mechanical properties of friction stir processed NiAl bronze, Mater. Sci. Eng., A 524 (2009) 119–128.
[7] D.R. Ni, B.L. Xiao, Z.Y. Ma, Y.X. Qiao, Y.G. Zheng, Corrosion properties of friction–stir processed cast NiAl bronze, Corros. Sci. 52 (2010) 1610–1617.
[8] A. Schüssler, H.E. Exner, The corrosion of nickel–aluminium bronzes in seawater-I. Protective layer formation and the passivation mechanism, Corros. Sci. 34 (1993) 1793–1802.
[9] A. Schüssler, H.E. Exner, The corrosion of nickel–aluminium bronzes in seawater-II. The corrosion mechanism in the presence of sulphide pollution, Corros. Sci. 34 (1993) 1803–1815.
[10] J.A. Wharton, K.R. Stokes, The influence of nickel–aluminium bronze microstructure and crevice solution on the initiation of crevice corrosion, Electrochim. Acta 53 (2008) 2463–2473.
[11] A. Al-Hashem, W. Riad, The role of microstructure of nickel–aluminium–bronze alloy on its cavitation corrosion behavior in natural seawater, Mater. Charact. 48 (2002) 37–41.
[12] R.C. Barik, J.A. Wharton, R.J.K. Wood, K.S. Tan, K.R. Stokes, Erosion and erosion–corrosion performance of cast and thermally sprayed nickel–aluminium bronze, Wear 259 (2005) 230–242.
[13] V. Guillaumin, P. Schmutz, G.S. Frankel, Characterization of corrosion interfaces by the scanning Kelvin probe force microscopy technique, J. Electrochem. Soc. 148 (2001) B163–B173.
[14] A.B. Cook, Z. Barrett, S.B. Lyon, H.N. McMurray, J. Walton, G. Williams, Calibration of the scanning Kelvin probe force microscope under controlled environmental conditions, Electrochim. Acta 66 (2012) 100–105.
[15] T.H. Muster, A.E. Hughes, Applications and limitations of scanning Kelvin probe force microscopy for the surface analysis of aluminum alloys, J. Electrochem. Soc. 153 (2006) B474–B485.
[16] A. Davoodi, J. Pan, C. Leygraf, S. Norgren, The role of intermetallic particles in localized corrosion of an aluminum alloy studied by SKPFM and integrated AFM/SECM, J. Electrochem. Soc. 155 (2008) C211–C218.
[17] S. Neodo, D. Carugo, J.A. Wharton, K.R. Stokes, Electrochemical behaviour of nickel–aluminium bronze in chloride media: influence of pH and benzotriazole, J. Electroanal. Chem. 695 (2013) 38–46.
[18] M. Sababi, S. Ejnermark, J. Andersson, P.M. Claesson, J. Pan, Microstructure influence on corrosion behavior of a Fe–Cr–V–N tool alloy studied by SEM/EDS, scanning Kelvin force microscopy and electrochemical measurement, Corros. Sci. 66 (2013) 153–159.
[19] H. Stanislaw, D. Tomasz, Work functions of elements expressed in terms of the Fermi energy and the density of free electrons, J. Phys.: Condens. Matter 10 (1998) 10815.
[20] M. Jönsson, D. Thierry, N. LeBozec, The influence of microstructure on the corrosion behaviour of AZ91D studied by scanning Kelvin probe force microscopy and scanning Kelvin probe, Corros. Sci. 48 (2006) 1193–1208.
[21] C.H. Tang, F.T. Cheng, H.C. Man, Effect of laser surface melting on the corrosion and cavitation erosion behaviors of a manganese–nickel–aluminium bronze, Mater. Sci. Eng., A 373 (2004) 195–203.
[22] B.G. Ateya, E.A. Ashour, S.M. Sayed, Corrosion of α-Al bronze in saline water, J. Electrochem. Soc. 141 (1994) 71–78.
[23] F. King, C.D. Litke, M.J. Quinn, D.M. LeNeveu, The measurement and prediction of the corrosion potential of copper in chloride solutions as a function of oxygen concentration and mass-transfer coefficient, Corros. Sci. 37 (1995) 833–851.
[24] A. Davoodi, J. Pan, C. Leygraf, S. Norgren, In situ investigation of localized corrosion of aluminum alloys in chloride solution using integrated EC-AFM/SECM techniques, Electrochem. Solid-State Lett. 8 (2005) B21–B24.
[25] A. Davoodi, J. Pan, C. Leygraf, S. Norgren, Integrated AFM and SECM for in situ studies of localized corrosion of Al alloys, Electrochim. Acta 52 (2007) 7697–7705.
[26] J. Izquierdo, L. Nagy, S. González, J.J. Santana, G. Nagy, R.M. Souto, Resolution of the apparent experimental discrepancies observed between SVET and SECM for the characterization of galvanic corrosion reactions, Electrochem. Commun. 27 (2013) 50–53.